Reconstruction of the plasmasphere from Moon-based EUV images

Fei He,[1] Xiao-Xin Zhang,[2] Bo Chen,[1] and Mei-Ching Fok[3]

Received 9 December 2010; revised 23 August 2011; accepted 25 August 2011; published 5 November 2011.

[1] A two-step algorithm for plasmasphere reconstruction from images obtained from the Moon-based extreme ultraviolet (EUV) imager on the Chang'e-3 mission is described and illustrated using simulation data obtained from a dynamic global core plasma model (DGCPM). According to the line of sight (LOS) integration patterns in Moon-based EUV imaging and the outline characteristics of the images, the equatorial plane plasmapause is reconstructed with the Minimum L Algorithm by adopting a magnetic dipole approximation. Having obtained the plasmapause locations, the quasi three-dimensional (3-D) plasmasphere, which is put into the Genetic Algorithm (GA) as an initial guess, is constructed with a statistical model assuming that the density along a field line is a constant. In this way, the plasmaspheric structure and the quasi 3-D plasmaspheric density are extracted from the Moon-based EUV images. This work provides a feasible and applicable method for data analysis of Moon-based EUV imaging, which is to be realized on the Chang'e-3 mission in the Second Phase of Chinese Lunar Exploration Program.

Citation: He, F., X. X. Zhang, B. Chen, and M.-C. Fok (2011), Reconstruction of the plasmasphere from Moon-based EUV images, *J. Geophys. Res.*, *116*, A11203, doi:10.1029/2010JA016364.

1. Introduction

[2] The torus-shaped plasmasphere is a cold and dense plasma region in the Earth's inner magnetosphere, which corotates with the Earth [*Sandel et al.*, 2003; *Burch et al.*, 2004; *Gallagher et al.*, 2005; *Galvan et al.*, 2010]. The particles in the plasmasphere are trapped on the magnetic field lines forming a field-aligned distribution, for which an empirical field-aligned density model suitable for constructing the realistic global plasmasphere model has been established by *Tu et al.* [2006]. The outer boundary of the plasmasphere is called the plasmapause, where the plasma density drops dramatically by 1–2 orders of magnitude or more in a relatively short distance of ~0.5 R_E (Earth radii) [*Carpenter*, 1963, 1966; *Gringauz*, 1963; *Carpenter and Anderson*, 1992]. The shape and geocentric distance of the plasmapause are highly dependent on the interplanetary and geomagnetic conditions [e.g., *Grebowsky*, 1970; *Horwitz et al.*, 1990; *Carpenter and Anderson*, 1992; *Moldwin et al.*, 2002; *Larsen et al.*, 2007], and it is usually located at geocentric distances of 3.0–6.0 R_E on magnetic equatorial plane [*Lemaire and Gringauz*, 1998; *Sandel et al.*, 2003].

[3] In the past two decades, many remote sensing methods have been developed and applied to the plasmasphere [e.g., *Carpenter*, 2004, and references therein], among which EUV photon imaging (NOZOMI-XUV [*Nakamura et al.*, 2000]; IMAGE-EUV [*Sandel et al.*, 2000]; KAGUYA-TEX [*Yoshikawa et al.*, 2008]) has been proved to be the most effective method to obtain the global external views of the plasmasphere. The EUV images are collected through detecting the resonantly scattered solar 30.4 nm radiation by plasmaspheric He^+ with the intensity proportional to the column integrated density of the He^+ along the LOS, given that the plasmasphere is optically thin to 30.4 nm radiation [*Brandt*, 1961; *Meier and Weller*, 1972; *Garrido et al.*, 1994]. Since He^+ is the second most abundant ion (constitutes approximately 15% of the total plasma population [*Craven et al.*, 1997]) in the plasmasphere, measurements of the He^+ density can be used as a proxy of the overall plasmasphere.

[4] In the Second Phase of the Chinese Lunar Exploration Program, which will be implemented in 2013, an EUV camera with field of view (FOV) of 16°, angular resolution of 0.095°, and time resolution of ~10 min will be mounted outside the instrumental module on the top of the lunar lander of the Chang'e-3 Mission (CE-3) to image the 30.4 nm radiation scattered from the Earth's plasmasphere and then to study the dynamics of the plasmasphere from a new perspective. The Moon-based EUV camera is able to detect intensities less than 0.1 Rayleigh and to capture the global structures of the plasmasphere (e.g., plasmapause, plume, shoulder, etc.).

[5] One significant characteristic of the EUV images is the sharp He^+ edge; i.e., the boundary of the bright pixels and dim pixels. *Goldstein et al.* [2003] studied the Radio Plasma Imager (RPI) [*Reinisch et al.*, 2000] and EUV [*Sandel et al.*, 2000] data from the IMAGE mission [*Burch*, 2000] and revealed that the sharp He^+ edge in EUV images can be

[1]Changchun Institute of Optics, Fine Mechanics and Physics, Chinese Academy of Sciences, Changchun, China.
[2]National Center for Space Weather, China Meteorological Administration, Beijing, China.
[3]NASA Goddard Space Flight Center, Greenbelt, Maryland, USA.

0148-0227/11/2010JA016364

reliably interpreted as the plasmapause. Thus, knowing the two-dimensional (2-D) plasmapause on the equatorial plane from the EUV images serves as a basis from which one can reconstruct a 3-D plasmapause by utilizing an empirical magnetic field model [*Wang et al.*, 2006]. Meanwhile, large scale plasmaspheric features including shoulders, plumes, notches, etc. [*Sandel et al.*, 2001, 2003; *Goldstein et al.*, 2002; *Gallagher et al.*, 2005] can be identified on the equatorial plane. The plasmapause has other uses; such as serving as an indicator of geomagnetic activity [*Goldstein et al.*, 2003; *Spasojević et al.*, 2003] or as an input parameter of plasmasphere model [*Carpenter and Anderson*, 1992].

[6] The Edge Algorithm first proposed by *Roelof and Skinner* [2000] is a pure geographical approach to retrieve the equatorial plane plasmapause shape from IMAGE-EUV images [*Sandel et al.*, 2001] without any minimization calculations. However, this algorithm has three limitations according to *Wang et al.* [2007]. First, it assumes that the plasmapause intersects the equatorial plane only once for a certain MLT; however, when a wrapped plume exists, there may be three intersections for some MLTs. Second, in some cases there is no envelope for certain LOS curves, such as notch and plume regions. Third, it is hard to find the exact envelope for the LOS curves in practice when the plasmapause is highly irregular. A revised Edge Algorithm proposed by *Wang and Newman* [2004] solves the first limitation by using a multiple crossing region hypothesis. Based on this algorithm, *Wang et al.* [2007] proposed the Minimum L Algorithm, which can solve the above problems. Details of the algorithm will be introduced in section 3.

[7] The pseudo-density inversion technique of *Gallagher et al.* [2005] is used to obtain He^+ density distribution from EUV images. Their technique is based on the concept that the innermost regions penetrated by a given LOS will contribute most to the observed 30.4 nm intensity due to rapidly falling densities in the plasmasphere with increasing L-shell [*Sandel et al.*, 2003]. The EUV instrument counts are first converted to column integrated density, and then the column integrated density is converted to pseudo-density by dividing by an estimate of the distance along the LOS that contributes most to the image intensity at each location in the FOV. The limiting factor of the technique is the extent of the error bars associated with the He^+ density of any given pixel. Most inverted densities are within about 50% of original with the maximum errors at the sharp plasmapause, in the Earth's shadow and in the low density channel inside the wrapped plume. In fact, this technique can be used to estimate density variations in plasma content and to capture the plasmaspheric features from EUV images.

[8] The iterative inversion approach proposed by *Gurgiolo et al.* [2005] is the first effort to perform a "true" inversion of the 2-D IMAGE-EUV images. In their approach, the equatorial plane He^+ density is represented by a density matrix, each element of which represents a grid point in this plane parameterized in L-value (L) and geomagnetic longitude (Λ) and is associated with one LOS of the EUV image. This approach has been proven applicable to imaging geometries that project the plasmaspheric emissions on the equatorial plane. In perspectives like Moon-based EUV imaging, the plasmaspheric emission is projected on different meridian planes for different lunar positions and all the lines of sight are associated with different L-values and geomagnetic latitudes. Since some lines of sight of a Moon-based EUV image are parallel to the equatorial plane and have no associated gird point on the equatorial plane, the approach proposed by *Gurgiolo et al.* [2005] cannot be directly used to invert the Moon-based EUV images.

[9] The above mentioned algorithms are all applied to the EUV images collected at high geomagnetic latitudes from the IMAGE EUV Imager operating in an Earth's polar orbit. This paper focuses on the reconstruction of the plasmapause from EUV images collected at very low latitudes (usually less than 15°) from lunar orbit. The arrangement of the paper is as follows. In section 2, the EUV imageries from the Earth's polar orbit and lunar orbit are presented and some limitations in the Moon-based EUV images are discussed. Then the Minimum L Algorithm and its application to Moon-based EUV images are introduced in detail in section 3. In section 4, the *Carpenter and Anderson* [1992] density model (CA Model) is used as a test for the applicability of the algorithm. In section 5, reconstruction results of the plasmapause for 24 May 2000 (Storm-I) and 26 June 2000 (Storm-II) storms modeled by the DGCPM [*Ober et al.*, 1997] are presented and analyzed. The inversion of the plasmaspheric density with a genetic algorithm (GA) will be presented in section 6. Finally, a discussion and summary will be given in section 7.

2. EUV Imaging From Polar Orbit and Lunar Orbit

[10] In the case of plasmasphere, where the plasma is constrained to dipole or dipole-like field lines, two typical projections are usually employed, one is to project the plasmaspheric emissions on the equatorial plane, and the other is to project them on meridian planes, as are shown in Figure 1a. Owing to the limitations of image FOV, the images can only by obtained from the apogee region when the imager is operating in the Earth's polar orbit. In this viewing geometry, there is a unique LOS that is tangent to the plasmapause surface for a given MLT, and the outline in the EUV image is more or less the same as the shape of the equatorial plasmapause. Figures 1b–1d show three types of plasmasphere in birdcage format. Figure 1b represents the simplest plasmasphere without special features; Figure 1c shows the plasmasphere with wrapped plume and shoulder structures; and Figure 1d reveals the plasmasphere with unwrapped plume structure. The thick lines in Figures 1b–1d represent the intersection lines of the plasmapause surface to the equatorial plane (or equatorial plasmapause). The outlines for the three types of plasmasphere when imaged from position A_1 (North Pole) are shown in Figures 1e–1g. It is clear that the shapes of the plasmasphere outlines are almost the same as the equatorial plasmapause.

[11] However, the results are completely different from those obtained from the lunar perspective (e.g., CE-3 mission). If the imager is located in the region between the two dashed lines in Figure 1a (e.g., position C), the LOS can only be tangent to the plasmapause surface that faces the imager with the other side shaded, hence the imager should be located outside the dashed region; e.g., the positions of B_1, B_2, or B_3. When imaged from these positions, the plasmapause surface at each MLT has its own unique tangential LOS. During the first-quarter Moon to the last-quarter Moon

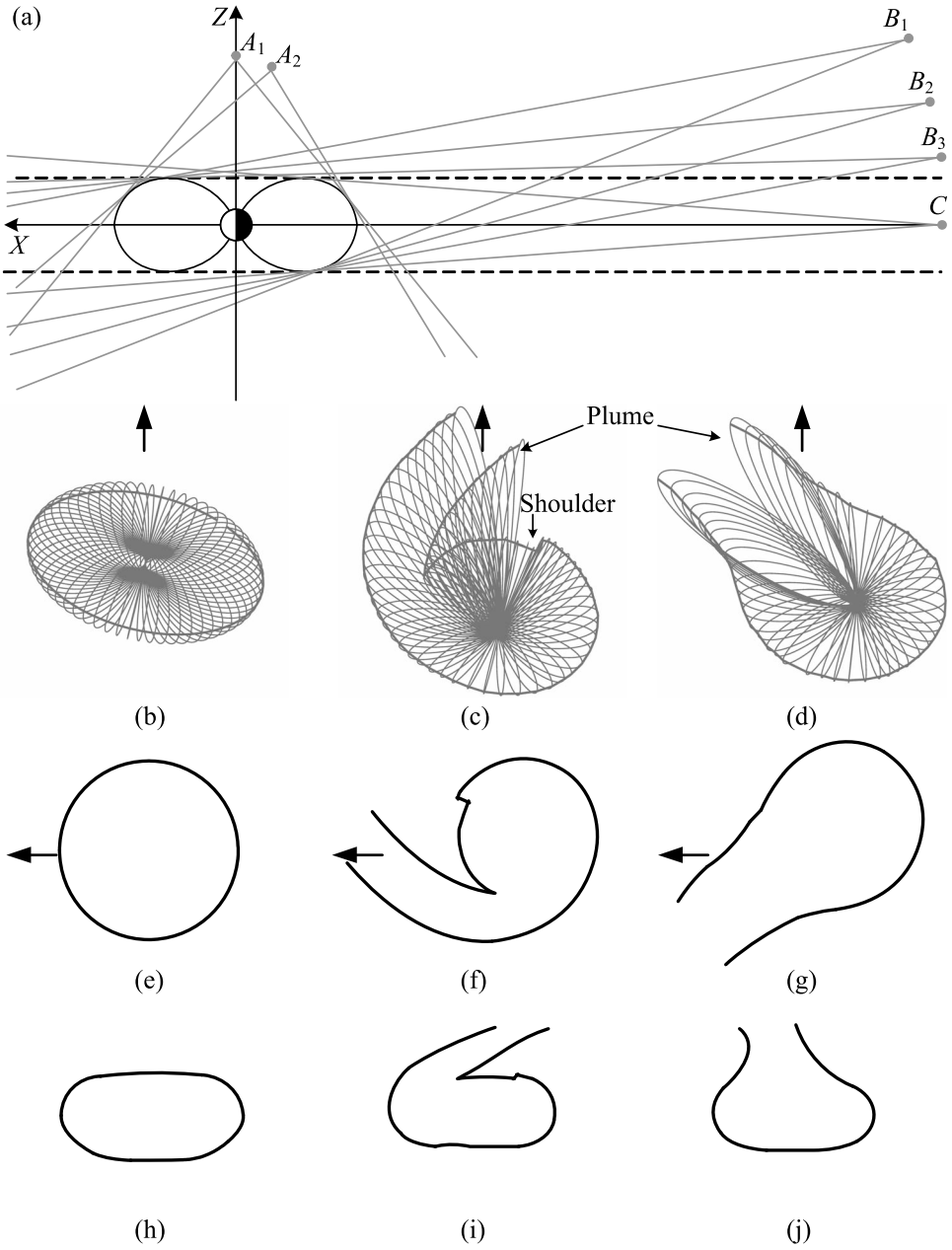

Figure 1. Image the plasmasphere from polar orbit and lunar orbit. (a) Illustration of the LOSs (gray lines) that are tangent to the plasmapause surface from different positions in polar orbit and lunar orbit, and the *L*-value of the dipole field line is 5.0. (b–d) Bird cage rendering of the plasmapause. (e–g) The plasmasphere outline on EUV image obtained from position A_1. (h–j) The plasmasphere outline on EUV image obtained from position B_2. The bold arrows in Figures 1b–1g represent the directions of the sun.

(here it represents half of the lunar orbit centered on 00:00 MLT from Earth's perspective), the Moon is above the equatorial plane of SM coordinate system and the unique tangential LOS condition can be satisfied. The plasmasphere outlines imaged from position B_2 are shown in Figures 1h–1j for the three types of plasmasphere, respectively. It is obvious that all these outlines are totally different from the equatorial plasmapause shapes.

[12] Since there is no plasmaspheric EUV image simultaneously (e.g., stereo) detected from different perspectives (e.g., Polar and Lunar), it is difficult to reconstruct plasmaspheric density from single images with traditional approaches, including the computerized tomographic (CT) method [*Kak and Slaney*, 1999] and algebraic reconstruction technique (ART) [*Gordon et al.*, 1970; *Herman et al.*, 1973; *Andersen and Kak*, 1984]. However, the quasi 3-D plasmasphere can be reconstructed by adding some constraints, including fixing the plasmapause locations at different longitudes and assuming the density along a field line to be constant.

[13] Reconstruction of the equatorial plane plasmapause from EUV images collected by the IMAGE mission has been done by *Roelof and Skinner* [2000], *Sandel et al.* [2003], *Wang and Newman* [2004], *Gurgiolo et al.* [2005], and *Wang et al.* [2007]. However, reconstruction from EUV images

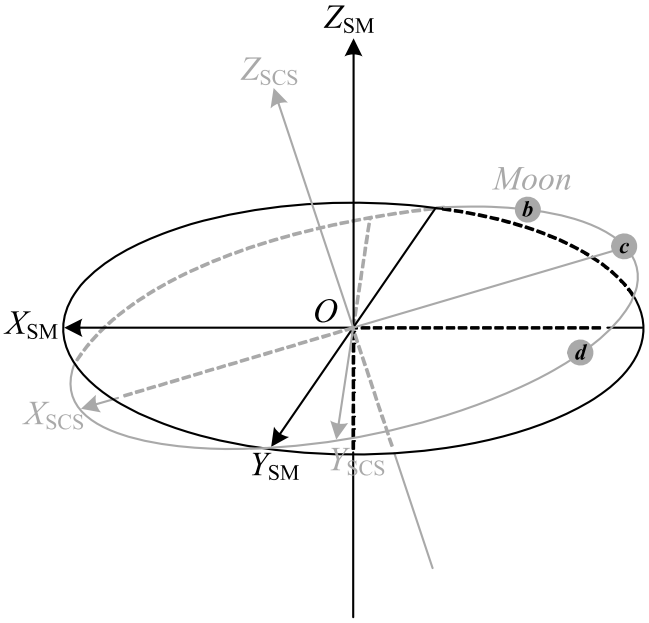

Figure 2. Illustration of the SM (black) and SCS (gray) coordinate systems. O is the Earth's center, X_{SM}-O-Y_{SM} is the equatorial plane, and X_{SCS}-O-Y_{SCS} is the lunar orbit. The three gray circles labeled b, c, and d represent the positions of the Moon used in section 5.

detected from lunar perspective still needs to be investigated. The Minimum L Algorithm proposed by *Wang et al.* [2007] solves the limitations of former algorithms (Edge Algorithm) and obtains fine results for the images obtained from polar perspectives. The Minimum L Algorithm will be introduced in detail and its applicability to lunar perspective images will be discussed next.

3. Minimum L Algorithm

3.1. Algorithm Overview

[14] The rationality, accuracy, and suitability of the Minimum L Algorithm have been discussed in detail by *Roelof and Skinner* [2000], *Sandel et al.* [2001], and *Wang et al.* [2007]. Here we just state the steps of the algorithm. The algorithm implementation is divided into four steps as follows:

[15] 1. The first step is to determine the pixel whose LOS goes through the center of the Earth (center pixel). This pixel is used as a reference for other pixels during the calculation of the LOS vectors.

[16] 2. After the determination of the center pixel, the second step is to calculate the LOS vectors for each plasmasphere outline pixel based on the parameters of the center pixel, angular resolution of the sensor, and the sensor location information.

[17] 3. The third step is to calculate the L-values of all the dipole field lines intersected by the LOS through a plasmasphere outline pixel. For all the field lines, the one with the minimum L-value is identified, while the L-value (L) and geomagnetic longitude (Φ) of the line are saved. After all the plasmasphere outline pixels are processed, the coordinate tuples (L, Φ) on the equatorial plane are determined.

[18] 4. Finally, the coordinate tuples are interpolated with B-Spline to form a smooth curve representing the equatorial plane plasmapause.

3.2. Application to Moon-Based Images

[19] In the construction of the Moon-based EUV images, a virtual EUV imager is located on the surface of the Moon viewing toward the center of the Earth, and moves with the Moon. The spatial resolution of the imager is 0.1 R_E (the corresponding angular resolution is 0.095° with the average Moon-Earth distance assumed to be 60.0 R_E) on the projection plane, which crosses the center of the Earth and is perpendicular to the axis of FOV; the temporal resolution is 10 min, during which the angle generated due to lunar motion is ~0.08°, which is less than the angular resolution of 0.095°, and the motion of plasmasphere is less than 0.1 R_E [*Goldstein et al.*, 2003; *Murakami et al.*, 2007]; thus the motions of the Moon and the plasmasphere are both ignored. The image FOV is 16.0° × 16.0° corresponding to a spatial area of 16.0 R_E × 16.0 R_E on the projection planes.

[20] The SM coordinate system is adopted in the DGCPM and the coordinates of the Moon are transformed to the SM coordinate system. In the construction of the Moon-based EUV images, for convenient expression and easy calculations of LOS vectors, a satellite coordinate system (SCS) is set up based on the SM coordinate system, as is shown in Figure 2. The axis of the imager's FOV (or Moon-Earth line) is set to be the x axis of SCS (X_{SCS}). Given the position of the Moon in actual conditions, the longitude and latitude of X_{SCS} in SM coordinate system are calculated. Then the two angles are used to rotate the Y_{SM} and Z_{SM} to get Y_{SCS} and Z_{SCS} respectively, which form an orthogonal system satisfying the right hand law with X_{SCS}. The Z_{SCS} is parallel to the lunar orbital axis and the SCS coordinate system changes with the Moon. The column integrations are done and the LOS vectors are calculated in SCS. All the EUV images below are projected on the $X = 0$ plane of SCS.

[21] The Moon-based EUV images are 161 × 161 pixels in the $X = 0$ plane of SCS (namely the projection plane). According to the above settings, the Earth center is represented by the central pixel (the 81st pixel in both horizontal and vertical directions), corresponding to the origin (0.0, 0.0, 0.0) in SCS. If a plasmasphere outline pixel is (N, M) in the image, the coordinate of this pixel is $\mathbf{P_P}$ = (0.0, (N-81) × 0.1 R_E, (M-81) × 0.1 R_E), in which 0.1 represents the spatial resolution on the projection plane. The coordinate of the imager in SCS is $\mathbf{P}_S$ = (-R_S, 0.0, 0.0), where R_S is set to be 60.0 R_E (while R_S is determined by imager-to-Earth distance in real images). Finally, the LOS vector $\mathbf{V_{LOS}}$ is determined ($\mathbf{V_{LOS}} = \mathbf{P}_P - \mathbf{P}_S$).

[22] In the construction of the LOS curves on the SM equatorial plane, each point in the LOS with interval of 0.05 R_E is first transformed to SM coordinate system, then the L-value and longitude of the dipole field line passing this point are determined. As to all the dipole field lines touched by the LOS, the one with minimum L-value is identified and the polar coordinate (L, Φ) of its intersection point on the equatorial plane is saved. When all the plasmasphere outline pixels are processed, the curve $L(\Phi)$ representing the plasmapause on the SM equatorial plane is determined. Finally, the equatorial plasmapause is reconstructed through B-Spline interpolation of the tuples (L, Φ) to get a

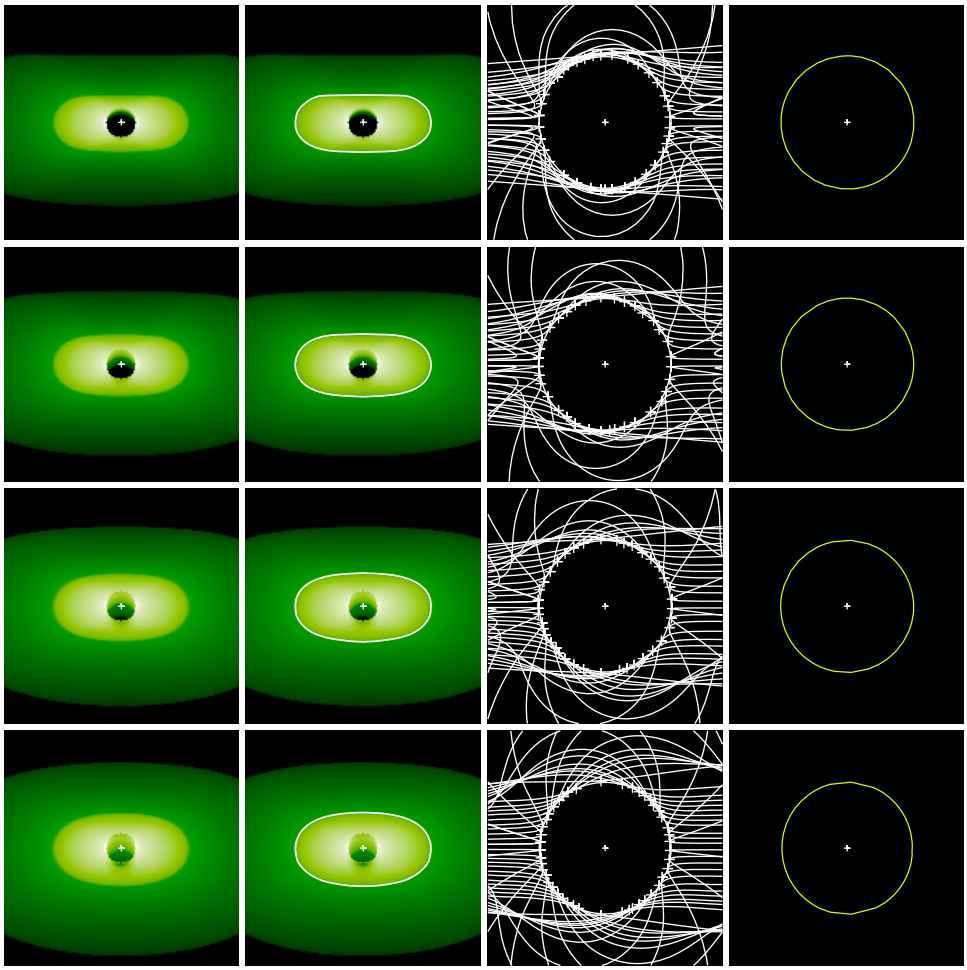

Figure 3. Minimum L algorithm applied to CA model. From top to bottom, the EUV images in first column are collected at latitudes of 4°, 8°, 12°, and 16°. The second column shows the plasmasphere outlines (white curves) overlaid in the modeled images. Third column shows the LOS curves on equatorial plane. Fourth column shows the reconstructed equatorial plane plasmapause (yellow). The white plus signs located at the center of the each image represent the center of the Earth.

smooth curve. In the above procedures, all LOSs are assumed to be single crossing, while multiple crossing cases [*Wang et al.*, 2007] will be considered in section 5.

4. CA Model Tests

[23] As a validation of the Minimum L Algorithm applied to the Moon-based plasmaspheric EUV images, the CA Model [*Carpenter and Anderson*, 1992] is adopted. With a magnetic dipole approximation, the 3-D plasmaspheric density is computed by tracing the field lines to the magnetic equatorial plane where the density is calculated by the CA Model. It is assumed that the plasmasphere is azimuthally symmetric for simplicity. The standard plasmapause position used in this section is set to be 4.5 R_E. Since the CA Model is an equatorial electron density model, two further steps are necessary to construct the hypothesis plasmasphere for EUV imaging.

[24] The first step is to transform the electron density (n_e) to He^+ density (n_{He}). The electron density is assumed to be equal to the sum density of He^+ and H^+ for the electric neutrality in plasmasphere ignoring O^+ whose concentration is very low [*Comfort et al.*, 1988; *Gallagher et al.*, 2000]. The relative concentration ($\alpha_{He/H}$) of He^+ to H^+ ions in the plasmasphere can be calculated with the empirical model of *Craven et al.* [1997]. Finally, the He^+ density can be obtained by $n_{He} = n_e\alpha_{He/H}/(1+\alpha_{He/H})$.

[25] Then, the remaining step is to construct the 3-D plasmaspheric density. It is assumed that the He^+ density along a magnetic field line is a constant. While several field-aligned plasmaspheric density models exist [*Gallagher et al.*, 2000; *Huang et al.*, 2004; *Tu et al.*, 2006], the assumption employed here is that the field-aligned He^+ density is constant. This is a reasonable assumption since most of the flux tube volume is near the equatorial plane. This assumption also makes the calculations of the 3-D plasmaspheric density and the weight matrix simpler and more efficient. The magnetic dipole field is used to map the 3-D space onto the equatorial plane. In addition, the SM coordinate system is adopted in our calculations, and the dipole tilt angle is ignored thereafter.

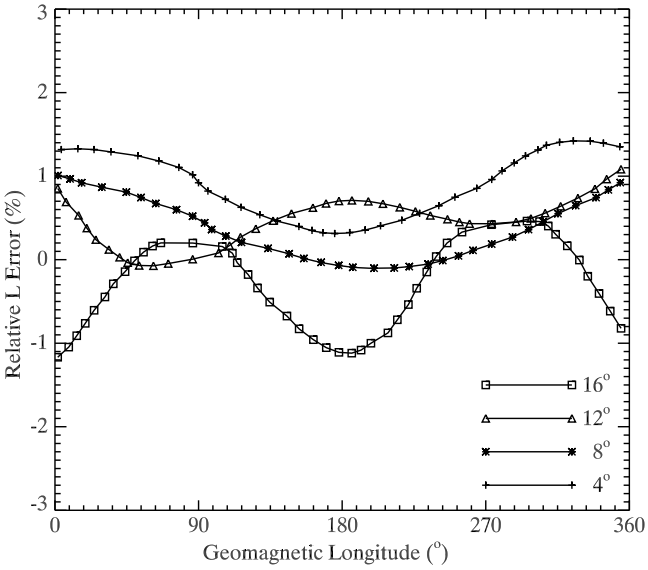

Figure 4. Illustration of relative L error for the reconstructed equatorial plasmapause.

[26] After the construction of the 3-D plasmasphere, the plasmaspheric EUV images can be modeled with the following integration equation:

$$I = \frac{10^{-6}}{4\pi} \int_{\ell} \exp(-\tau) p(\theta) g n(\mathbf{r}) ds \qquad (1)$$

where I denotes the emission intensity in Rayleighs, $p(\theta) = 1 + 1/4(2/3\text{-}\sin^2\theta)$ is the phase function reflecting the anisotropy of scattered radiation [*Brandt and Chamberlain*, 1959], θ is the angle between the incident direction (Sun-Earth direction) and the scattered direction (from the scattering point to the imager), g is the resonant scattering rate (photons s^{-2} ion^{-1}) calculated with the method involved in *Garrido et al.* [1994], $n(\mathbf{r})$ is the He^+ density in cm^{-3} at position $\mathbf{r}$, and τ is the optical depth of 30.4 nm line, which can be assumed to be zero since the absorption of magnetospheric species to 30.4 nm radiation is extremely low above 1000 km [*Brandt*, 1961; *Garrido et al.*, 1994], ℓ is the integration path along a LOS, and ds is the integration element.

[27] Here, only one geomagnetic longitudinal position of the Moon (at midnight in SM coordinate system) is adopted since the plasmapause is assumed to be azimuthally symmetric. The latitudes of the Moon in the SM coordinate system range from 4° to 16° with an increment of 4°. Actually, when the imager is located at midnight (full Moon sector of lunar orbit), the major radiation in the FOV is the solar radiation, and the imager must be shut down. In the test of the Minimum L Algorithm with the CA model, the influence of the sun is ignored. For the "real" plasmasphere to be discussed in section 5, direct sunlight is avoided in selection of the lunar positions.

[28] The Minimum L Algorithm applications to CA Model are shown in Figure 3. For the four latitudes (4°, 8°, 12°, and 16°), the equatorial plane plasmapause can be well reconstructed from Moon-based EUV images. As is shown in Figure 4, the maximum relative error of the reconstructed plasmapause is 1.5%, corresponding to an absolute error of about 0.07 R_E (from the standard plasmapause at 4.5 R_E).

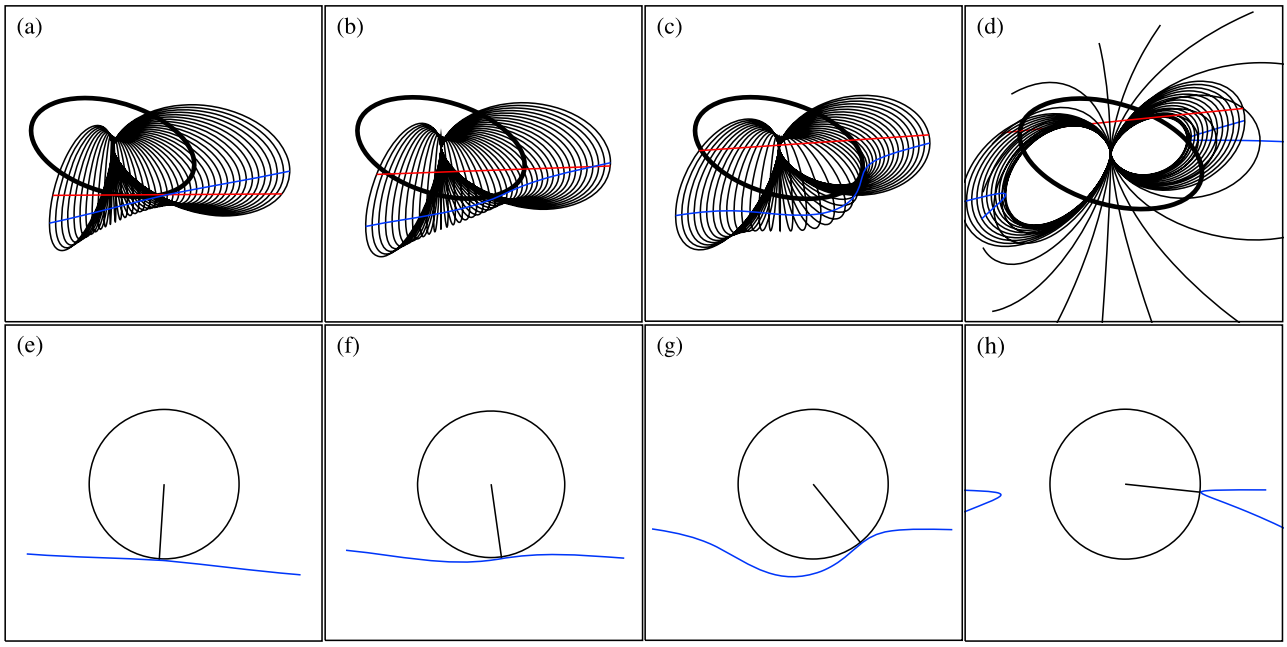

Figure 5. Four types of LOS curves in Moon-based EUV images as are shown in Figure 3. Radial lines in Figures 5e–5h correspond to the minimum L points. The Ω type line LOS curves in Figures 5d and 5h are not displayed completely. Red line indicates LOS, blue line indictes LOS curve, black line indicates dipole field lines touched by these LOS. The dashed circles in Figures 5a–5d and solid circles in Figures 5e–5h represent the standard plasmapause (4.5 R_E).

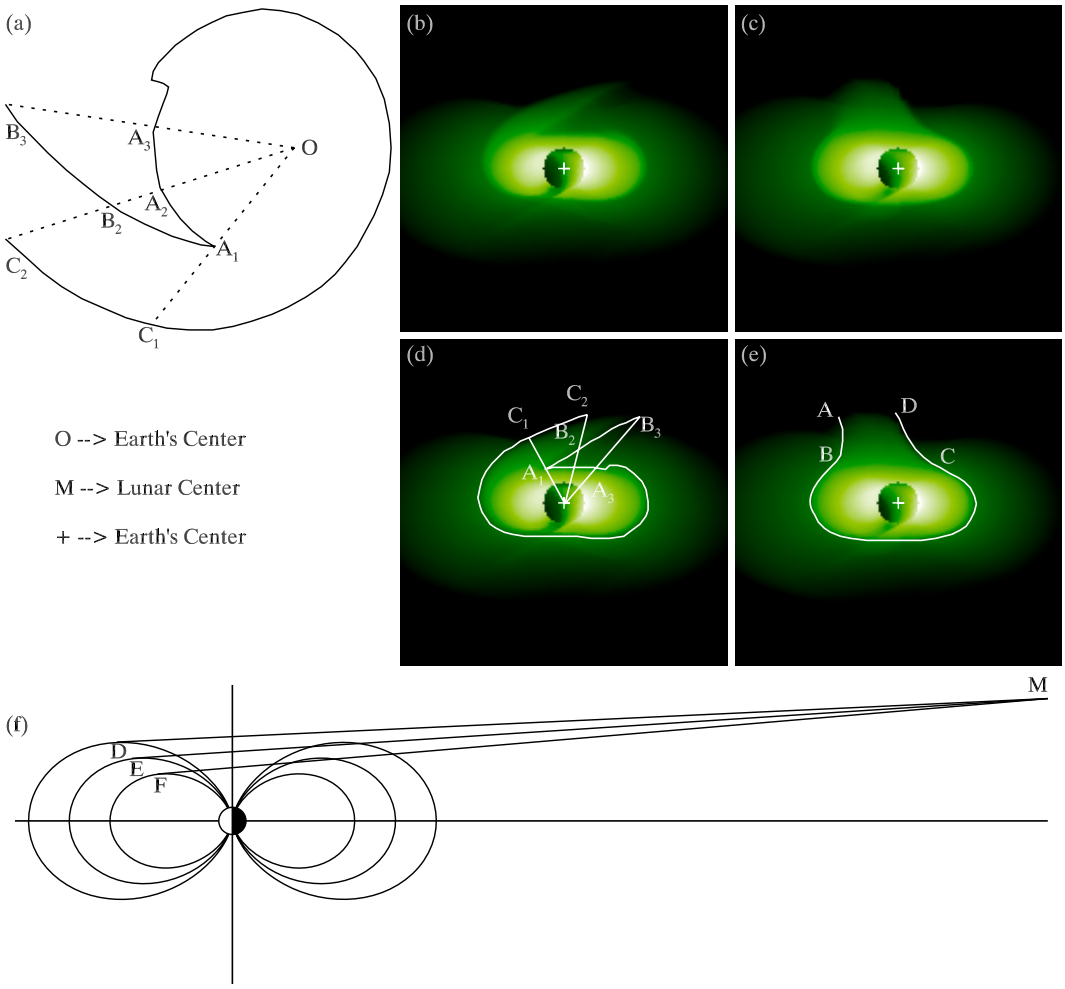

Figure 6. Illustration of multiple crossing region. (a) Equatorial plane plasmapause multiple crossing regions, (b–c) plasmaspheric images of Storm-I and Storm-II, (d–e) plasmaspheric outlines (white curves) overlaid in the images of Storm-I and Storm-II, and (f) illustration of three LOSs that are tangent to the plasmapause of the multiple crossing region.

[29] As are shown in Figure 3, there are four types of LOS curves (presented in Figure 5) whose tangential lines coincide with the tangential lines of the plasmapause surface. When the LOS is tangent to the low-latitude plasmapause surface (corresponding to the plasmasphere outline pixels at the right edge in each plot of the second column in Figure 3), the intersection points to the dipole field lines are near the SM equatorial plane with little latitudinal change (Figure 5a), and the LOS curves are more or less like a "straight line" (Figure 5e). As the plasmasphere outline pixel moves to the upper center, the LOS is tangent to the high-latitude plasmapause surface, especially near polar region (Figure 5d), the latitude of the dipole field lines touched by the LOS change from 62–~80° and the corresponding L-values change from 4.5–~40.0, forming a "Ω type line" LOS curve (Figure 5h).

[30] Tests of the algorithm with the CA Model show that Minimum L Algorithm is absolutely applicable to Moon-based plasmaspheric EUV images. Next, we will investigate the applications of the algorithm to more complex plasmaspheres with plume and shoulder structures, and further discuss the multiple crossing problems.

5. "Real" Plasmasphere

[31] The "real" plasmaspheric structures simulated by the DGCPM are more complex than those simulated by the CA Model. When there are plumes, shoulders, notches, or other structures in the plasmasphere, the reconstruction procedures will become more complex. We will encounter a multiple crossing problem, namely, the plasmapause intersects the equatorial plane multiple times (usually three times) for certain MLTs. As is shown in Figure 6a, the plasmapause intersects the equatorial plane for three times at points A_2, B_2, and C_2.

[32] Commonly, the plasmasphere has a wrapped or unwrapped plume on the dayside while the nightside plasmapause is more or less like a circular arc. Thus the reconstruction of the nightside plasmapause is straightforward, while the reconstruction of the dayside plasmapause

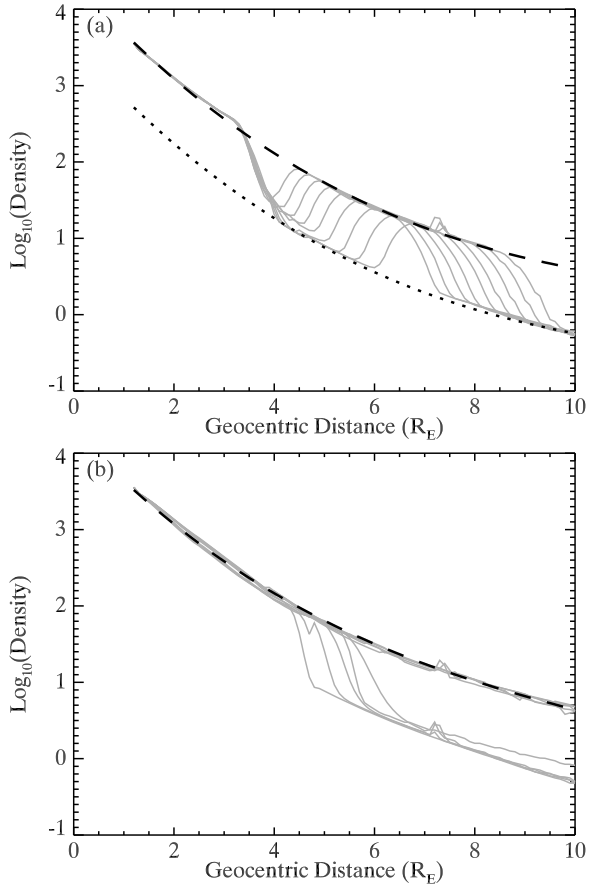

Figure 7. Comparisons of plasmaspheric density to plume density showing (a) Storm-I and (b) Storm-II. Gray curves are density modeled by DGCPM. The dashed curves are fitted density profiles for the main plasmasphere and the plume. The dotted line represents the fitted density profile for the trough between plasmapause and inner boundary of the plume and the trough outside the outer boundary of the plume.

(boundary of the plume or shoulder) is comparatively laborious. For the plume region, the first step is to identify the boundaries of the plume in the Moon-based EUV images. As is shown in Figure 7, the density distribution (the solid gray lines) in the main plasmasphere obeys almost the same law (the dashed black lines) as the plumes for both storms. For wrapped plumes (Figure 7a), the density between the plasmapause (line segment A_1–A_2 in Figure 6a) and the inner boundary of the plume (line segment A_1–B_2 in Figure 6a), and the density outside the outer boundary of the plume (line segment C_1–C_2) are both low and behave the same law (the dotted black line).

[33] For the multiple crossing region, the LOS (e.g., MF in Figure 6f) that go through the pixels on line segment A_1–A_3 are tangent to the plasmapause of the main plasmasphere, the LOS (e.g., ME in Figure 6f) that go through the pixels on line segment A_1–B_3 are tangent to the inner boundary of the plume, and the LOS (e.g., MD in Figure 6f) that go through the pixels on line segment C_1–C_2 are tangent to the outer boundary of the plume.

[34] Another troublesome problem we will encounter is the Earth's shadow. As is shown by IMAGE mission observations [*Sandel et al.*, 2003] and model simulations [*He et al.*, 2010], the Earth's shadowing is apparent when observed from polar orbit, and the nightside plasmapauses in polar EUV images are difficult to identify. In Moon-based EUV images; however, the Earth's shadowing has little effect on the determination of plasmasphere outline in the image. What mainly affects the determination of plasmasphere outline is the shading (or overlapping) of the main plasmasphere. For example, when the imager is located at the first-quarter Moon or last-quarter Moon sector of lunar orbit, the plume or shoulder structures may be shaded by the main plasmasphere, which makes the determination of the outline of the plume or shoulder impossible. When the imager is located near the full Moon sector of lunar orbit, the shading of the main plasmasphere has little effect on plasmasphere outline determination.

[35] Thus in this study, three positions *b*, *c*, and *d* located near the full Moon sector of lunar orbit in Figure 2 are adopted. Their coordinates in SM are *b* (−39.7 R_E, −40.8 R_E, 9.5 R_E), *c* (−51.3 R_E, −21.9 R_E, 12.2 R_E), and *d* (−51.4 R_E, 21.9 R_E, 11.9 R_E), respectively. At these positions, the solar 30.4 nm radiations have no influence on Moon-based EUV imaging since the angle between the axis of the FOV (16.0° × 16.0°) of the imager and the Sun-Earth line is greater than 16.0°, thus no solar radiation can directly enter the imager.

[36] For Storm-I, the plasmasphere outline pixels in single crossing regions (line segments A_1–A_3 and A_3–C_1 in Figure 6d) are used to reconstruct the plasmapause of the main plasmasphere; the plasmasphere outline pixels on line segment C_1–C_2 are used to reconstruct the outer boundary of the plume; and the plasmasphere outline pixels on line segment A_1–B_3 are used to reconstruct the inner boundary of the plume. For Storm-II, the plasmasphere outline pixels on line segment B–C in Figure 6e are used to reconstruct the plasmapause of the main plasmasphere; and the plasmasphere outline pixels on line segments A–B and C–D are used to reconstruct the boundaries of the plume.

[37] The reconstruction results for Storm-I and Storm-II are presented in Figure 8. The standard plasmapause is extracted from the equatorial density distribution simulated by DGCPM. The maximum and average relative errors of the reconstructed equatorial plane plasmapause are 0.08 R_E and 0.01 R_E, respectively.

6. Inversion of Plasmaspheric Density

[38] After determination of the equatorial plane plasmapause, the plasmaspheric density can, theoretically, be derived from an inversion of equation (1). Since it is impossible to analytically solve this nonlinear integral equation, a search and optimization method is necessary. In this respect, GA is the best choice.

6.1. Basic Principles of GA

[39] GA is an efficiently heuristic overall optimization searching algorithm first invented by Holland [*Holland*, 1975]. It is the most popular technique in evolutionary computation and is highly developed in artificial intelligence [*Reeves and Rowe*, 2003; *Sivanandam and Deepa*, 2008, and references therein]. GA is a kind of algorithm that draws

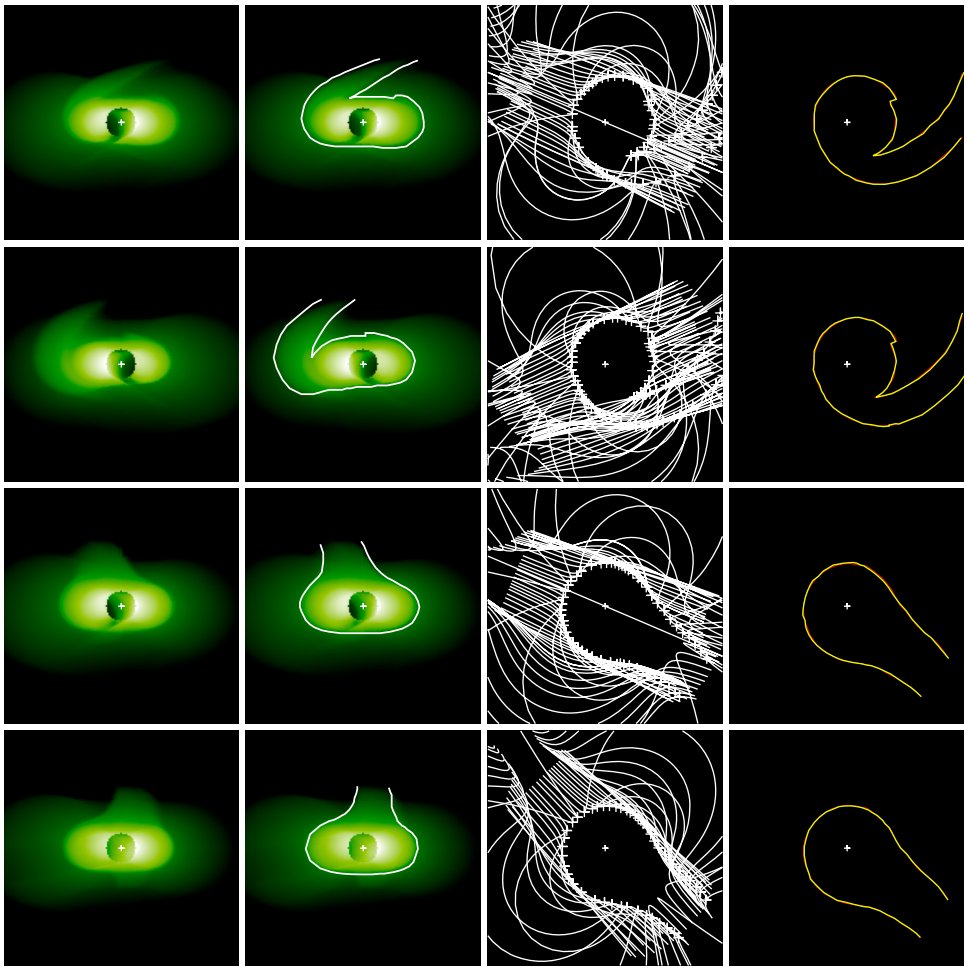

Figure 8. Equatorial plasmapause reconstructed from Moon-based EUV images. Top row shows Storm-I EUV image detected at position c. Second row shows Storm-I EUV image detected at position d. Third row shows Storm-II EUV image detected at position c. Bottom row shows Storm-II EUV image detected at position b. First column shows Moon-based EUV images. Second column shows EUV images with plasmasphere outline overlaid. Third column shows LOS curves on equatorial plane. Fourth column shows comparison of reconstructed plasmapause (yellow) and standard plasmapause (red). The white plus signs located at the center of the images represent the center of the Earth.

lessons from the Darwinian evolution of heredity, crossover, mutation, selection, and "Survival of the Fittest." The goal of the GA approach is to replicate the theory of natural selection mathematically.

[40] The GA begins with a population that represents the potential solution set of the problem to be solved. This population is composed of a certain number of individuals after gene coding. Just like an individual in nature, the individual in GA displays fractional characteristics of the solution of the problem. The individuals are coded as binary or float strings (also called chromosome) according to specific problems. The float coding GA (FCGA), coding the individuals as real vectors or matrices [*Michalewicz*, 1996], is adopted here since the solution of our problem belongs to the set of real numbers. The space of all feasible solutions forms the search space. For scalar problems, the solution is a float number, and then the search space is the set of real numbers. For vector problems, the solution is a real vector or a 2-D curve, and then the search space is a 2-D space of real numbers. For matrix problems, the solution is a real matrix or a 3-D curved surface, and then the search space is a 3-D space of real numbers.

[41] GA has been successfully applied to optimization problems like wire routing, scheduling, adaptive control, game playing, cognitive modeling, transportation problems, traveling salesman problems, optimal control problems, database query optimization, etc. [see *Michalewicz*, 1996; *Sivanandam and Deepa*, 2008, and references therein]. It can be used here to invert the plasmaspheric density from Moon-based EUV images.

[42] Searching for the best solution is equivalent to looking for the extreme of a function in the search space. To achieve this, reproduction and selection of the individuals are performed. Just like the evolution of living creatures through crossover, mutation, and selection, the individuals in GA evolve to optimal solution through these procedures. Crossover and mutation represent different mathematical operations on the father chromosomes. The former is used to interchange the information of the father chromosomes

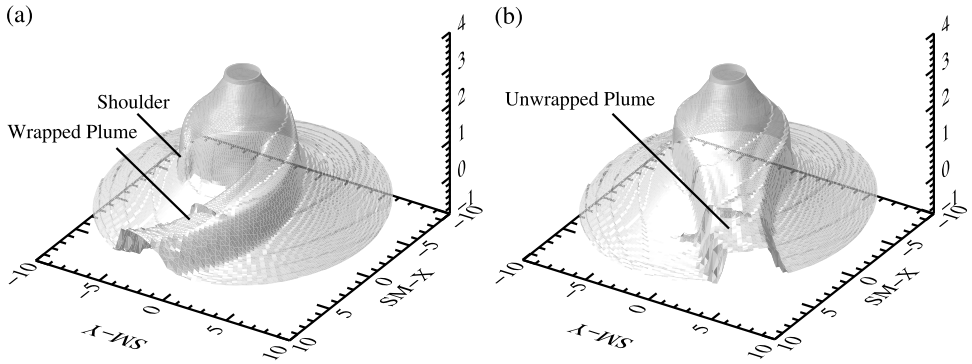

Figure 9. Equatorial plane plasmaspheric density distributions from DGCPM showing (a) Storm-I and (b) Storm-II. Z axis is the log density of the plasmasphere.

and the latter to introduce new information in the son chromosomes.

[43] During the evolution we encounter the problems of evaluating the quality of the individuals and updating the population. This is accomplished by calculating the fitness value of the individual as well as by selection. Finally, when the fitness value reaches the prefixed threshold, the optimized solution of the problem is searched out.

[44] Inversion of the plasmaspheric density can be achieved through an optimization of the function:

$$f[n(\mathbf{r})] = I - \int_{\ell} \exp(-\tau) p(\theta) g n(\mathbf{r}) ds \times 10^{-6}/4\pi \qquad (2)$$

where $f[n(\mathbf{r})]$ is called target function, other variables are the same as those of equation (1) except that $n(\mathbf{r})$ is unknown. Our goal is to search for a best solution $n(\mathbf{r})$ that satisfies the condition of $f[n(\mathbf{r})] < e$ (a prefixed threshold, e.g., $e = 10^{-6}$ or smaller) in a 3-D space of real numbers. FCGA is used to search for the minimum of the function $f[n(\mathbf{r})]$. The implementation of the FCGA requires the steps to be described in sections 6.2–6.5.

6.2. Weight Matrix

[45] Since it is impossible to invert the 3-D plasmaspheric density $n(\mathbf{r})$ directly from equation (1), discretization of the integration equation and some simplifications are necessary. The 3-D density is converted to quasi 3-D. In order to achieve this, the target density grids are first set on the equatorial plane, and the meridian plane density is calculated by field line tracing assuming that the density along a field line is constant. The simple dipole field model is adopted since Earth's dipolar magnetic field is dominant in the plasmasphere region. Finally, the plasmaspheric density is represented by a 2-D matrix **N** defined on equatorial plane. Then the weight matrix is defined as follows.

[46] For a given LOS, the phase function $p(\theta)$ and the scattering factor g are both constant for all the points in the LOS. The column integration intensity of the LOS is determined by the density along the LOS curve on the equatorial plane. Given the integration elements ds, equation (1) can be rewritten as

$$I = c \sum_{i,j} W_{i,j} N_{i,j} \qquad (3)$$

where $c = p(\theta) g ds/4\pi \times 10^{-6}$ is a constant, $W_{i,j}$ is the element of the weight matrix **W**, and $N_{i,j}$ is the element of the density matrix **N**. If we set a polar grid on the equatorial plane with the dimensions of N_r (radial) × N_p (longitudinal), the dimensions of **W** will also be $N_r \times N_p$. Each element $W_{i,j}$ of the weight matrix represents the contribution of the density of the corresponding grid point to the intensity and is initialized to zero. All of the integration points along the LOS are mapped onto the equatorial plane. If the resultant point coincides with the grid point, then the value of the corresponding element of **W** is set to be 1.0; if not, the density of the resultant point is obtained by 2-D interpolation, and the interpolation coefficients are allocated to the corresponding elements of **W**.

[47] Since different LOSs correspond to different LOS curves on the equatorial plane (see Figures 3 and 8), each

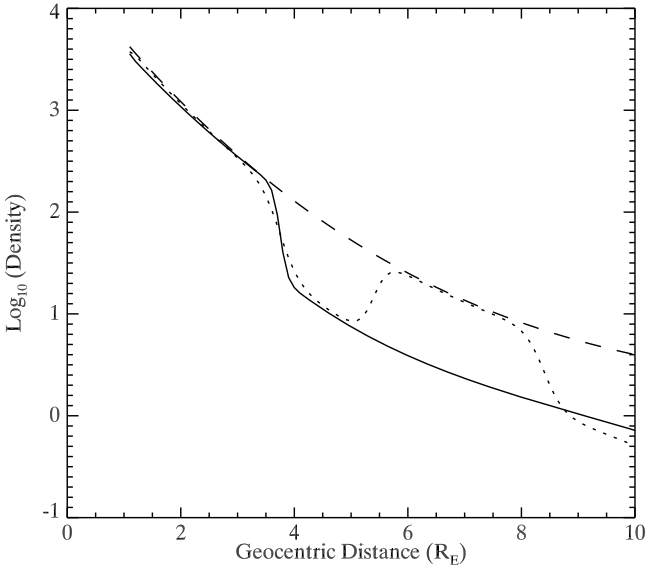

Figure 10. Three types of plasmaspheric density structures extracted from Figure 9. The solid line is obtained by cutting the plasmasphere without crossing the plume in Figure 9. The dotted line is obtained by cutting the plasmasphere crossing the wrapped plume in Figure 9a. The dashed line is obtained by cutting the plasmasphere within the unwrapped plume in Figure 9b.

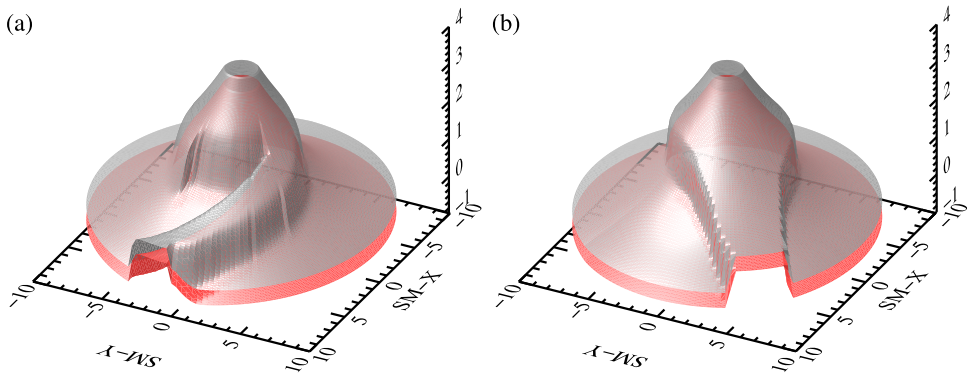

Figure 11. Boundary conditions and algorithm search space for FCGA showing (a) Storm-I and (b) Storm-II. Z axis is the log density of the plasmasphere. Gray layer is the upper boundary, and red layer is the lower boundary.

pixel in the Moon-based EUV image has its own weight matrix. Thus equation (3) should be rewritten as

$$I_{i,j} = \sum_{kl} W_{ij,kl} N_{kl} \tag{4}$$

where (i, j) denotes the index of a pixel in the image, (k, l) denotes the index of a point in the density grid, and the constant c has been multiplied to $W_{ij,kl}$. If the dimension of the EUV image is $N_h \times M_v$, then there are $N_h \times M_v$ weight matrixes with the dimension of $N_r \times N_p$.

6.3. Coding of the Chromosomes

[48] Just like the individuals in nature, the chromosome is the basic unit in GA. For plasmaspheric inversion, the chromosome is represented by the density matrix **N** of the plasmasphere. The elements of **N** represent the density values of the corresponding grids. The coding of the chromosomes, initial values, and the boundary conditions define the search space of GA. So coding is very important in GA. The density feature of the plasmasphere decides the coding mode and the boundary conditions.

[49] The plasmaspheric He^+ densities range from 0.1 cm^{-3} in plasma trough region to several 1000 cm^{-3} in the inner plasmasphere. There are many types of density structures in the plasmasphere, e.g., shoulder [*Goldstein et al.*, 2002], wrapped plume [*Sandel et al.*, 2003], corotating notch [*Gallagher et al.*, 2005], corotating density trough [*Carpenter et al.*, 2000; *Adrian et al.*, 2001; *Fu et al.*, 2010], erosion event [*Goldstein*, 2006], etc. Figure 9 shows two examples of plasmaspheric density distributions from DGCPM simulations, which are also commonly observed [e.g., *Sandel et al.*, 2003; *Spasojević et al.*, 2003] and simulated [e.g., *Grebowsky*, 1970; *Chen and Wolf*, 1972; *Ober et al.*, 1997; *Liemohn et al.*, 2004] before. There are sharp plasmapause, wrapped plume, and shoulder structures in the plasmasphere in Figure 9a, whereas only sharp plasmapause and unwrapped plume structures in the plasmasphere are presented in Figure 9b. For the DGCPM under consideration in this work, we only consider the typical structures of plasmapause, shoulder, and plume in the plasmasphere.

[50] As is shown in Figures 9 and 10, we consider three basic plasmaspheric density distributions. Using a radial meridian plane to cut the surfaces in Figure 9, we get three types of plasmaspheric density profiles in Figure 10. The first type has *single plasmapause* (solid line in Figure 10), corresponding to the plasmasphere without crossing the plume in Figure 9. The second type has *single plasmapause and two plume boundaries* (dotted line in Figure 10), corresponding to the plasmasphere crossing the wrapped plume in Figure 9a. The third type has *no plasmapause* (dashed line in Figure 10), corresponding to the plasmasphere within the unwrapped plume in Figure 9b. Above three basic types

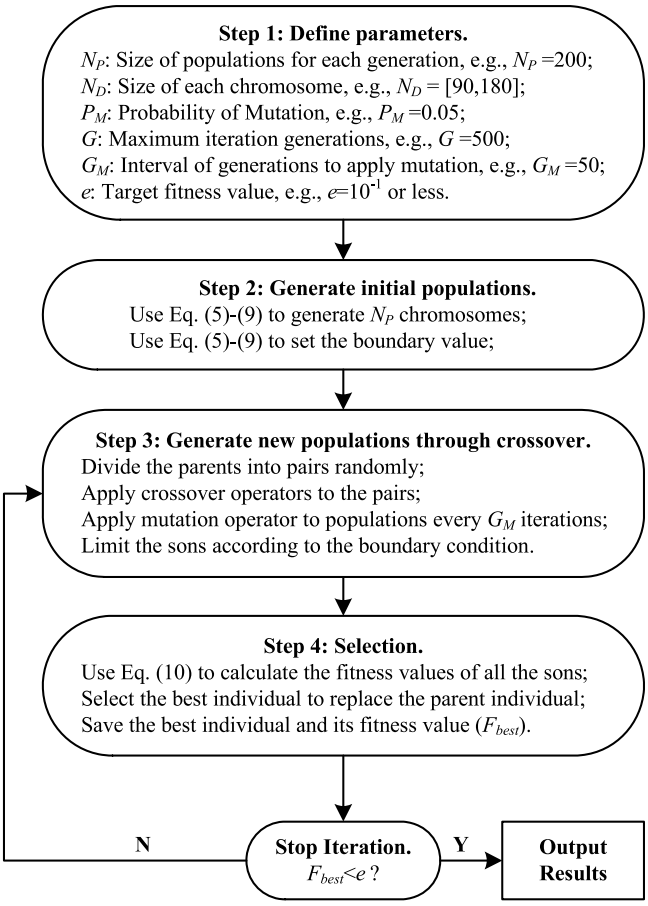

Figure 12. Flowchart of the FCGA.

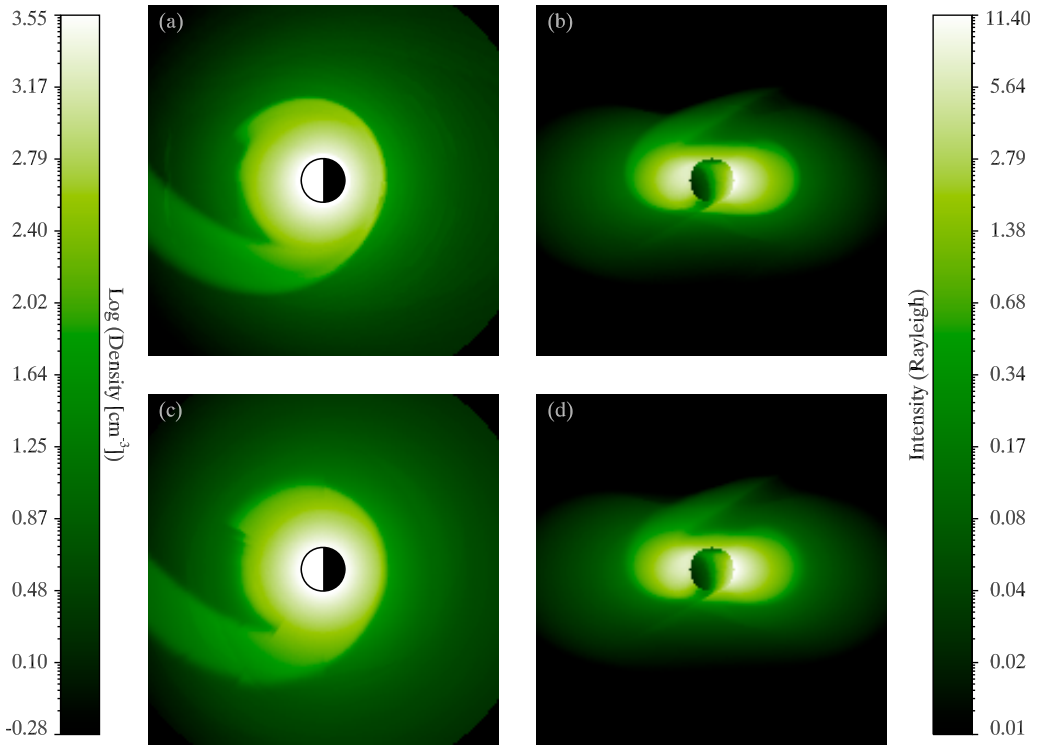

Figure 13. Reconstruction results for Storm-I: (a) standard plasmaspheric density, (b) standard image, (c) reconstructed plasmaspheric density, and (d) reconstructed image. The log-scaled color bar for the density is shown at left, and the log-scaled color bar for the intensity is shown at right.

of density profiles may not completely or truly reveal all the plasmaspheric density distributions and they are just used for the convenient construction of the initial chromosomes and search space in FCGA.

[51] In construction of the initial chromosomes, the density profiles for the main plasmasphere and the plume are the same, and the density profile for the trough between the plasmapause and the inner boundary of the plume is the same as that of the trough outside the outer boundary of the plume. Based on the plasmaspheric density data from the DGCPM simulations under different geomagnetic activities (weak, median, and strong), the density profiles for the main plasmasphere $n_{Main}(r)$ and the plume $n_{Plume}(r)$ are fitted as follows with least square polynomial fitting:

$$\log_{10}[n_{Main}(r)] = -0.001r^3 + 0.0455r^2 - 0.7325r + 4.355 \quad (5)$$

$$\log_{10}[n_{Plume}(r)] = -0.001r^3 + 0.0455r^2 - 0.7325r + 4.355 \quad (6)$$

where r is the geocentric distance in R_E on equatorial plane. The density profile for the trough $n_{Trough}(r)$ is

$$\log_{10}[n_{Trough}(r)] = -0.0034r^3 + 0.0925r^2 - 0.9773r + 3.967 \quad (7)$$

Density profiles of the different regions are integrated by a switch function $f(r, \varphi)$:

$$f(r,\varphi) = \tanh(a(\varphi)(x - b(\varphi)))/2.0 + 0.5 \quad (8)$$

where r is geocentric distance, φ is longitude, $a(\varphi)$ controls the switching region of the two adjacent models, and $b(\varphi)$ controls the connecting center, which is determined by the plasmapause reconstructed in sections 4 and 5. The value of $a(\varphi)$ has been fitted to be 6.0 at nightside and 4.0 at dayside. Finally, the equatorial plane density $N(r, \varphi)$ is constructed by

$$N(r,\varphi) = n(r)f(r,\varphi) \quad (9)$$

where $n(r)$ is the density calculated by equations (5) to (7), $f(r, \varphi)$ is the switch function. Using the fitted models and the plasmaspheric boundary conditions (plasmapause), the equatorial plane plasmaspheric density matrix **N** is constructed, and the upper and lower boundaries are set by adding or subtracting a constant to **N**. With this method, the search space (see Figure 11) of the FCGA is greatly contracted and the convergency of the FCGA is improved.

6.4. Reproduction of Chromosomes

[52] After coding the chromosomes, we need to define the reproduction rules of the chromosomes. Reproduction rules that determine how the next generation is produced are core elements of the GA. The chromosomes are reproduced in two ways. One is crossover between two chromosomes and the other is the mutation of a single chromosome. Some information is inherited from the father; some information of the father is discarded. Among the sons, some are good, others are bad, and their survival is determined by the rule of "Survival of the Fittest," which is realized through selection rules to be described next. We have designed six types of

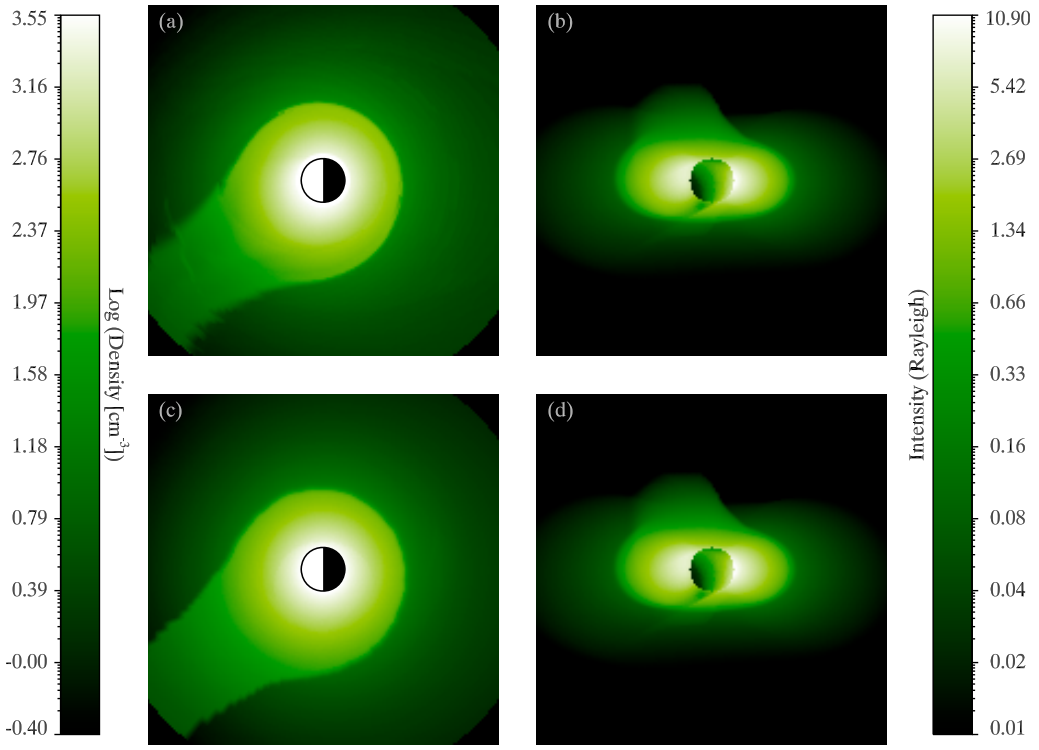

Figure 14. Reconstruction results for Storm-II: (a) standard plasmaspheric density, (b) standard image, (c) reconstructed plasmaspheric density, and (d) reconstructed image. The log-scaled color bar for the density is shown at the left, and the log-scaled color bar for the intensity is shown at right.

crossover operators and one mutation operator (see Appendix A for details). The parents are randomly divided into pairs first, and then the crossover operators are applied to each pair to produce new populations. A mutation operator is applied to the new populations every few iterations according to the mutation probability.

6.5. Selection Rule

[53] The final step is to define the selection rules of the son generation. It is essential in GA to retain the good populations and discard the bad ones of the son generation. The core of the selection rule is the selection criterion. In our study, the criterion (or the fitness) of an individual is defined as

$$F = \sum_{i=1}^{N_h} \sum_{j=1}^{M_v} \left(I_{ij} - \sum_{k=1}^{N_r} \sum_{l=1}^{N_p} W_{ij,kl} N_{kl} \right)^2 \qquad (10)$$

where F is the fitness value, and other variables have been defined before. The smaller the value of F is, the better the individual is. The steps of FCGA are presented in Figure 12.

Table 1. Relative Intensity Errors for the Reconstructed EUV Images

EUV Image	Maximum Error	Average Error	Standard Deviation
Storm-I	6.1×10^{-1}	3.94×10^{-2}	4.15×10^{-2}
Storm-II	7.2×10^{-1}	3.82×10^{-2}	4.96×10^{-2}

6.6. Application Results

[54] In the application of inversion, the DGCPM is first used to generate the original EUV images or the standard EUV images (Figures 13a, 13b, 14a, 14b), from which the equatorial plasmapause is derived with the Minimum L Algorithm. The EUV images in Figures 13 and 14 are both simulated at position c in Figure 2. The initial guesses of the density are obtained in Step 2 of Figure 12. Then these data are put into the FCGA for iteration. The reconstructed EUV images are shown in Figure 13d (for Storm-I) and Figure 14d (for Storm-II). For the two reconstructed images, the relative intensity error with the corresponding pixels of the standard image and the relative density error with the corresponding grid points of the standard plasmasphere are calculated. The results are presented in Tables 1 and 2. These errors suggest that the reconstructed plasmasphere densities are reasonable and credible.

7. Discussion and Conclusions

[55] We have used the Minimum L Algorithm to reconstruct the equatorial plane plasmapause from the Moon-based EUV images. For the plasmasphere with simple structures, the reconstruction of equatorial plane plasma-

Table 2. Relative Density Errors for the Reconstructed Plasmasphere

Plasmasphere	Maximum Error	Average Error	Standard Deviation
Storm-I	8.1×10^{-1}	4.94×10^{-2}	7.58×10^{-2}
Storm-II	7.2×10^{-1}	3.57×10^{-2}	7.63×10^{-2}

pause is easy and accurate. When there are complex structures, such as plume, shoulder, notch, and so on, the reconstruction procedure is complex. Currently, we can only reconstruct the plasmapause from Moon-based EUV images detected at specific positions in lunar orbit; e.g., from full Moon to last quarter Moon sector in lunar orbit.

[56] At other positions, owing to the shading of the main plasmasphere, some sectors of the plasmapause cannot be reconstructed, especially the special structures that we are interested in, such as the shoulder and the plume. A possibly feasible approach to identify the plasmasphere outline at this region is that one reconstructs the equatorial plasmapause of the main plasmasphere first, which is then used to construct a virtual image from the same position as the original image with the unclosed part of the plasmapause connected by a circular arc. The virtual image is subtracted from the original image to get a new image without shading of the main plasmasphere. The outline of the new image may be used to reconstruct the boundaries of the shoulder or the plume. This approach will be investigated in detail in future work.

[57] After the determination of the equatorial plane plasmapause, the plasmaspheric density is constructed with fitted models. Then this density is used as an initial guess for the GA to get the "real" plasmaspheric density iteratively. We have designed six types of crossover operators and one mutation operator for the reproduction of new individuals in GA. According to the principles of the GA, the best solution (density) with the EUV image constructed from which having the least difference from the original EUV image is searched out.

[58] Reconstruction results of the plasmasphere can be used to quantitatively study the dynamics of the plasmasphere. For example, (1) reconstruction of the plasmapause from a series of images can be used to monitor the evolution of the plasmapause and long period results can be used for statistical study of the relationships between plasmapause shapes and solar wind/interplanetary magnetic field; (2) the reconstructed boundaries and local time densities of plumes can be used to investigate the motions of the plume and to study the effect of the plumes on solar wind/magnetosphere coupling; (3) the reconstructed plasmaspheric densities as well as the equatorial plasmapause position can be used to derive the convection electric field from plasmaspheric Alfvén layer motions [*Larsen*, 2007]; and (4) the flux tubes' evolution as well as the latitudinal distribution of the flux tubes can be derived from series of the Moon-based EUV images, which helps us study the field-aligned density model of the plasmasphere.

[59] In our inversion algorithm, the density along field lines is set to be constant, which is not the real case. Therefore, the inversed density is pseudo 3-D. In future work, the field-aligned density model [e.g., *Tu et al.*, 2006] will be added to our algorithm to inverse true 3-D density distribution of the plasmasphere. If other EUV images from different perspectives (e.g., Earth's polar orbit) can be detected simultaneously, the three-dimensional density distribution can be reconstructed more accurately.

Appendix A: GA Operators

[60] In this section, **p** represents the fathers, **s** represents the sons, a (or **a**) represents the crossover factor, and the dimensions of **p** and **s** are both $N_r \times N_p$. The upper and lower boundaries of the populations are $\mathbf{b}''$ and $\mathbf{b}'$.

A1. Operator 1

[61] Generate a random number a between (0, 1), for $i = 1, N_r$ and $j = 1, N_p$

$$\begin{aligned} s^1_{i,j} &= a p^1_{i,j} + (1-a) p^2_{i,j} \\ s^2_{i,j} &= a p^2_{i,j} + (1-a) p^1_{i,j} \end{aligned} \tag{A1}$$

A2. Operator 2

[62] Generate random numbers a_j ($j = 1, N_p$) between (0, 1), and $a(j) = a(N_P)$, for $i = 1, N_r$ and $j = 1, N_p$

$$\begin{aligned} s^1_{i,j} &= a_j p^1_{i,j} + (1-a_j) p^2_{i,j} \\ s^2_{i,j} &= a_j p^2_{i,j} + (1-a_j) p^1_{i,j} \end{aligned} \tag{A2}$$

A3. Operator 3

[63] Generate random numbers a_{ij} ($i = 1, N_r, j = 1, N_p$) between (0, 1), and $a(i, j) = a(i, N_P)$, for $i = 1, N_r$ and $j = 1, N_p$

$$\begin{aligned} s^1_{i,j} &= a_{i,j} p^1_{i,j} + (1-a_{i,j}) p^2_{i,j} \\ s^2_{i,j} &= a_{i,j} p^2_{i,j} + (1-a_{i,j}) p^1_{i,j} \end{aligned} \tag{A3}$$

A4. Operator 4-1

[64] Generate random numbers k_j ($j = 1, N_p$, $1 \le k \le N_r$), generate a random number a between (0, 1), for $i = 1, N_r$ and $j = 1, N_p$

$$\begin{aligned} s^1_{i,j} &= \begin{cases} a p^1_{i,j} + (1-a) p^2_{i,j} & i = 1, \cdots, k_j \\ p^1_{i,j} & i = k_j + 1, \cdots, N_r \end{cases} \\ s^2_{i,j} &= \begin{cases} a p^2_{i,j} + (1-a) p^1_{i,j} & i = 1, \cdots, k_j \\ p^2_{i,j} & i = k_j + 1, \cdots, N_r \end{cases} \end{aligned} \tag{A4}$$

A5. Operator 4-2

[65] Generate random numbers k_j ($j = 1, N_p$, $1 \le k \le N_r$), generate a random number a between (0, 1), for $i = 1, N_r$ and $j = 1, N_p$

$$\begin{aligned} s^1_{i,j} &= \begin{cases} p^1_{i,j} & i = 1, \cdots, k_j \\ a p^1_{i,j} + (1-a) p^2_{i,j} & i = k_j + 1, \cdots, N_r \end{cases} \\ s^2_{i,j} &= \begin{cases} p^2_{i,j} & i = 1, \cdots, k_j \\ a p^2_{i,j} + (1-a) p^1_{i,j} & i = k_j + 1, \cdots, N_r \end{cases} \end{aligned} \tag{A5}$$

A6. Operator 5-1

[66] Generate random numbers k_j ($j = 1, N_p$, $1 \le k \le N_r$), generate random numbers a_j ($j = 1, N_p$) between (0, 1), for $i = 1, N_r$ and $j = 1, N_p$

$$s_{i,j}^1 = \begin{cases} a_j p_{i,j}^1 + (1 - a_j) p_{i,j}^2 & i = 1, \cdots, k_j \\ p_{i,j}^1 & i = k_j + 1, \cdots, N_r \end{cases}$$
$$s_{i,j}^2 = \begin{cases} a_j p_{i,j}^2 + (1 - a_j) p_{i,j}^1 & i = 1, \cdots, k_j \\ p_{i,j}^2 & i = k_j + 1, \cdots, N_r \end{cases} \quad \text{(A6)}$$

A7. Operator 5-2

[67] Generate random numbers k_j ($j = 1, N_p$, $1 \le k \le N_r$), generate random numbers a_j ($j = 1, N_p$) between (0, 1), for $i = 1, N_r$ and $j = 1, N_p$

$$s_{i,j}^1 = \begin{cases} p_{i,j}^1 & i = 1, \cdots, k_j \\ a_j p_{i,j}^1 + (1 - a_j) p_{i,j}^2 & i = k_j + 1, \cdots, N_r \end{cases}$$
$$s_{i,j}^2 = \begin{cases} p_{i,j}^2 & i = 1, \cdots, k_j \\ a_j p_{i,j}^2 + (1 - a_j) p_{i,j}^1 & i = k_j + 1, \cdots, N_r \end{cases} \quad \text{(A7)}$$

A8. Operator 6-1

[68] Generate random numbers k_j ($j = 1, N_p$, $1 \le k \le N_r$), generate random numbers a_{ij} ($i = 1, N_r$, $j = 1, N_p$) between (0, 1), for $i = 1, N_r$ and $j = 1, N_p$

$$s_{i,j}^1 = \begin{cases} a_{i,j} p_{i,j}^1 + (1 - a_{i,j}) p_{i,j}^2 & i = 1, \cdots, k_j \\ p_{i,j}^1 & i = k_j + 1, \cdots, N_r \end{cases}$$
$$s_{i,j}^2 = \begin{cases} a_{i,j} p_{i,j}^2 + (1 - a_{i,j}) p_{i,j}^1 & i = 1, \cdots, k_j \\ p_{i,j}^2 & i = k_j + 1, \cdots, N_r \end{cases} \quad \text{(A8)}$$

A9. Operator 6-2

[69] Generate random numbers k_j ($j = 1, N_p$, $1 \le k \le N_r$), generate random numbers a_{ij} ($i = 1, N_r$, $j = 1, N_p$) between (0, 1), for $i = 1, N_r$ and $j = 1, N_p$

$$s_{i,j}^1 = \begin{cases} p_{i,j}^1 & i = 1, \cdots, k_j \\ a_{i,j} p_{i,j}^1 + (1 - a_{i,j}) p_{i,j}^2 & i = k_j + 1, \cdots, N_r \end{cases}$$
$$s_{i,j}^2 = \begin{cases} p_{i,j}^2 & i = 1, \cdots, k_j \\ a_{i,j} p_{i,j}^2 + (1 - a_{i,j}) p_{i,j}^1 & i = k_j + 1, \cdots, N_r \end{cases} \quad \text{(A9)}$$

A10. Operator 7

[70] Generate random numbers a_{ij} ($i = 1, N_r$, $j = 1, N_p$) between (0, 1), for $i = 1, N_r$ and $j = 1, N_p$

$$s_{i,j} = \begin{cases} \begin{cases} p_{i,j} + \Delta\left(t, b_{i,j}^u - p_{i,j}\right), random(0,1) = 1 \\ p_{i,j} - \Delta\left(t, p_{i,j} - b_{i,j}^l\right), random(0,1) = 0 \end{cases} & \text{if } a_{i,j} < P_m \\ p_{i,j} & \text{if } a_{i,j} \ge P_m \end{cases} \quad \text{(A10)}$$

where P_m is the mutation probability, $\Delta(t, y) = y \times r \times (1 - t/T)^c$, r is a random number, T is the maximum iteration times, t is the current iteration times, c denotes the degree of non-uniformity [*Michalewicz*, 1996].

[71] **Acknowledgments.** This work is supported by the National Natural Science Foundation of China (grants 40890160, 10878004, and 40974093), the Major State Basic Research Development Program of China (973 Program) (Grant 2011CB811400), and the Special Fund for Public Welfare Industry (Grant GYHY200806024).

[72] Philippa Browning thanks the reviewers for their assistance in evaluating this manuscript.

References

Adrian, M. L., D. L. Gallagher, J. L. Green, B. R. Sandel, and M. F. Rose (2001), The large-scale plasmaspheric density trough associated with the 24 May 2000 geomagnetic storm: IMAGE EUV observations and Global Core Plasma Modeling, *Eos Trans. AGU*, *82*, S352.

Andersen, A. H., and A. C. Kak (1984), Simultaneous algebraic reconstruction technique (SART): A superior implementation of the ART algorithm, *Ultrason. Imaging*, *6*(1), 81–94, doi:10.1016/0161-7346(84)90008-7.

Brandt, J. C. (1961), Interplanetary gas, VI, on diffuse extreme ultraviolet helium radiation in the night and day sky, *Astrophys. J.*, *134*(2), 975–980, doi:10.1086/147225.

Brandt, J. C., and J. W. Chamberlain (1959), Interplanetary gas, I, hydrogen radiation in the night sky, *Astrophys. J.*, *130*(1), 670–682, doi:10.1086/146756.

Burch, J. L. (2000), IMAGE mission overview, *Space Sci. Rev.*, *91*(1–2), 1–14, doi:10.1023/A:1005245323115.

Burch, J. L., J. Goldstein, and B. R. Sandel (2004), Cause of plasmasphere corotation lag, *Geophys. Res. Lett.*, *31*, L05802, doi:10.1029/2003GL019164.

Carpenter, D. L. (1963), Whistler evidence of a "Knee" in the magnetospheric ionization density profile, *J. Geophys. Res.*, *68*(6), 1675–1682, doi:10.1029/JZ068i006p01675.

Carpenter, D. L. (1966), Whistler studies of the plasmapause in the magnetosphere, I. Temporal variations in the position of the knee and some evidence on plasma motions near the knee, *J. Geophys. Res.*, *71*(3), 693–709.

Carpenter, D. L. (2004), Remote sensing the Earth's plasmasphere, *Radio Sci. Bull.*, *308*, 13–29.

Carpenter, D. L., and R. R. Anderson (1992), An ISEE/whistler model of equatorial electron density in the magnetosphere, *J. Geophys. Res.*, *97*(A2), 1097–1108, doi:10.1029/91JA01548.

Carpenter, D. L., R. R. Anderson, W. Calvert, and M. B. Moldwin (2000), CRRES observations of density cavities inside the plasmasphere, *J. Geophys. Res.*, *105*, 23,323–23,338, doi:10.1029/2000JA000013.

Chen, A. J., and R. A. Wolf (1972), Effects on the plasmasphere of a time-varying convection electric field, *Planet. Space Sci.*, *20*(4), 483–509, doi:10.1016/0032-0633(72)90080-3.

Comfort, R. H., I. T. Newberry, and C. R. Chappell (1988), Preliminary statistical survey of plasmaspheric ion properties from observations by DE 1/RIMS, in *Modeling Magnetospheric Plasma*, edited by T. E. Moore and J. H. Waite Jr., pp. 107–114, AGU, Washington, D. C.

Craven, P. D., D. L. Gallagher, and R. H. Comfort (1997), Relative concentration of He^+ in the inner magnetosphere as observed by the DE 1 retarding ion mass spectrometer, *J. Geophys. Res.*, *102*(A2), 2279–2289, doi:10.1029/96JA02176.

Fu, H. S., J. Tu, J. B. Cao, P. Song, B. W. Reinisch, D. L. Gallagher, and B. Yang (2010), IMAGE and DMSP observations of a density trough inside the plasmasphere, *J. Geophys. Res.*, *115*, A07227, doi:10.1029/2009JA015104.

Gallagher, D. L., D. P. Craven, and R. H. Comfort (2000), Global core plasma model, *J. Geophys. Res.*, *105*(A8), 18,819–18,833, doi:10.1029/1999JA000241.

Gallagher, D. L., M. L. Adrian, and M. W. Liemohn (2005), Origin and evolution of deep plasmaspheric notches, *J. Geophys. Res.*, *110*, A09201, doi:10.1029/2004JA010906.

Galvan, D. A., M. B. Moldwin, B. R. Sandel, and G. Crowley (2010), On the causes of plasmaspheric rotation variability: IMAGE EUV observations, *J. Geophys. Res.*, *115*, A01214, doi:10.1029/2009JA014321.

Garrido, D. E., R. W. Smith, D. W. Swift, S.-I. Akasofu, R. M. Robinson, and Y. T. Chiu (1994), Imaging the plasmasphere and trough regions in the extreme ultraviolet region, *Opt. Eng.*, *33*(2), 371–382, doi:10.1117/12.155909.

Goldstein, J. (2006), Plasmasphere response: Tutorial and review of recent imaging results, *Space Sci. Rev.*, *124*, 203–216, doi:10.1007/s11214-006-9105-y.

Goldstein, J., R. W. Spiro, P. H. Reiff, R. A. Wolf, B. R. Sandel, J. W. Freeman, and R. L. Lambour (2002), IMF-driven overshielding electric field and the origin of the plasmaspheric shoulder of May 24, 2000, *Geophys. Res. Lett.*, *29*(16), 1819, doi:10.1029/2001GL014534.

Goldstein, J., M. Spasojević, P. H. Reiff, B. R. Sandel, W. T. Forrester, D. L. Gallagher, and B. W. Reinisch (2003), Identifying the plasmapause in IMAGE EUV data using IMAGE RPI in situ steep density gradients, *J. Geophys. Res.*, *108*(A4), 1147, doi:10.1029/2002JA009475.

Gordon, R., R. Bender, and G. T. Herman (1970), Algebraic reconstruction technique (ART) for three-dimensional electron microscopy and x-ray photography, *J. Theor. Biol.*, *29*, 471–481, doi:10.1016/0022-5193(70)90109-8.

Grebowsky, J. M. (1970), Model study of plasmapause motion, *J. Geophys. Res.*, *75*, 4329–4333, doi:10.1029/JA075i022p04329.

Gringauz, K. I. (1963), The structure of the ionized gas envelope of earth from direct measurements in the USSR of local charged particle concentrations, *Planet. Space Sci.*, *11*(3), 281–296, doi:10.1016/0032-0633(63)90030-8.

Gurgiolo, C., B. R. Sandel, J. D. Perez, D. G. Mitchell, C. J. Pollock, and B. A. Larsen (2005), Overlap of the plasmasphere and ring current: Relation to subauroral ionospheric heating, *J. Geophys. Res.*, *110*, A12217, doi:10.1029/2004JA010986.

He, F., X. X. Zhang, B. Chen, and M.-C. Fok (2010), Calculation of the extreme ultraviolet radiation of the Earth's plasmasphere, *Sci. China Technol. Sci.*, *53*(1), 200–205, doi:10.1007/s11431-009-0311-1.

Herman, G. T., A. Lent, and S. W. Rowland (1973), ART: Mathematics and applications, *J. Theor. Biol.*, *42*(1), 1–32, doi:10.1016/0022-5193(73)90145-8.

Holland, J. H. (1975), *Adaptation in Natural and Artificial Systems*, Univ. of Mich. Press, Ann Arbor.

Horwitz, J. L., R. H. Comfort, and C. R. Chappell (1990), A statistical characterization of plasmasphere density structure and boundary locations, *J. Geophys. Res.*, *95*, 7937–7947, doi:10.1029/JA095iA06p07937.

Huang, X., B. W. Reinisch, P. Song, J. L. Green, and D. L. Gallagher (2004), Developing an empirical density model of the plasmasphere using IMAGE/PRI observations, *Adv. Space Res.*, *33*(6), 829–832, doi:10.1016/j.asr.2003.07.007.

Kak, A. C., and M. Slaney (1999), *Principles of Computerized Tomograhic Imaging*, IEEE Press, New York.

Larsen, B. A. (2007), Quantitative studies of terrestrial plasmaspheric dynamics enabled by the IMAGE spacecraft, Ph.D. thesis, 130 pp., Montana State Univ., Bozeman.

Larsen, B. A., D. M. Klumpar, and C. Gurgiolo (2007), Correlation between plasmapause position and solar wind parameters, *J. Atmos. Sol. Terr. Phys.*, *69*(3), 334–340, doi:10.1016/j.jastp.2006.06.017.

Lemaire, J. F., and K. I. Gringauz (1998), *The Earth's Plasmasphere*, Cambridge Univ. Press, Cambridge, U. K., doi:10.1017/CBO9780511600098.

Liemohn, M. W., A. J. Ridley, D. L. Gallagher, D. M. Ober, and J. U. Kozyra (2004), Dependence of plasmaspheric morphology on the electric field description during the recovery phase of the 17 April 2002 magnetic storm, *J. Geophys. Res.*, *109*, A03209, doi:10.1029/2003JA010304.

Meier, R. R., and C. S. Weller (1972), EUV resonance radiation from helium atoms and ions in the geocorona, *J. Geophys. Res.*, *77*(7), 1190–1204, doi:10.1029/JA077i007p01190.

Michalewicz, Z. (1996), *Genetic Algorithms + Data Structures = Evolution Programs*, 3rd ed., Springer, Berlin.

Moldwin, M. B., L. Downward, H. K. Rassoul, R. Amin, and R. R. Anderson (2002), A new model of the location of the plasmapause: CRRES results, *J. Geophys. Res.*, *107*(A11), 1339, doi:10.1029/2001JA009211.

Murakami, G., M. Hirai, and I. Yoshikawa (2007), The plasmapause response to the southward turning of the IMF derived from sequential EUV images, *J. Geophys. Res.*, *112*, A06217, doi:10.1029/2006JA012174.

Nakamura, M., I. Yoshikawa, A. Yamazaki, K. Shiomi, Y. Takizawa, M. Hirahara, K. Yamashita, Y. Saito, and W. Miyake (2000), Terrestrial plasmaspheric imaging by an extreme ultraviolet scanner on Planet-B, *Geophys. Res. Lett.*, *27*(2), 141–144, doi:10.1029/1999GL010732.

Ober, D. M., J. L. Horwitz, and D. L. Gallagher (1997), Formation of density troughs embedded in the outer plasmasphere by subauroral ion drift events, *J. Geophys. Res.*, *102*(A7), 14,595–14,602, doi:10.1029/97JA01046.

Reeves, C. R., and J. E. Rowe (Eds.) (2003), *Genetic Algorithms—Principles and Perspectives: A Guide to GA Theory*, Kluwer Acad., Dordrecht, Netherlands.

Reinisch, B. W., et al. (2000), The Radio Plasma Imager investigation on the IMAGE spacecraft, *Space Sci. Rev.*, *91*, 319–359, doi:10.1023/A:1005252602159.

Roelof, E. C., and A. J. Skinner (2000), Extraction of ion distributions from magnetospheric ENA and EUV images, *Space Sci. Rev.*, *91*, 437–459, doi:10.1023/A:1005281424449.

Sandel, B. R., et al. (2000), The extreme ultraviolet imager investigation for the image mission, *Space Sci. Rev.*, *91*(1–2), 197–242, doi:10.1023/A:1005263510820.

Sandel, B. R., R. A. King, W. T. Forrester, D. L. Gallagher, A. L. Broadfoot, and C. C. Curtis (2001), Initial results from the IMAGE extreme ultraviolet imager, *Geophys. Res. Lett.*, *28*, 1439–1442, doi:10.1029/2001GL012885.

Sandel, B. R., J. Goldstein, D. L. Gallagher, and M. Spasojević (2003), Extreme ultraviolet imager observations of the structure and dynamics of the plasmasphere, *Space Sci. Rev.*, *109*(1), 25–46, doi:10.1023/B:SPAC.0000007511.47727.5b.

Sivanandam, S. N., and S. N. Deepa (2008), *Introduction to Genetic Algorithms*, Springer, New York.

Spasojević, M., J. Goldstein, D. L. Carpenter, U. S. Inan, B. R. Sandel, M. B. Moldwin, and B. W. Reinisch (2003), Global response of the plasmasphere to a geomagnetic disturbance, *J. Geophys. Res.*, *108*(A9), 1340, doi:10.1029/2003JA009987.

Tu, J.-N., P. Song, B. W. Reinisch, J. L. Green, and X.-Q. Huang (2006), Empirical specification of field-aligned plasma density profiles for plasmasphere refilling, *J. Geophys. Res.*, *111*, A06216, doi:10.1029/2005JA011582.

Wang, C., and T. S. Newman (2004), Improved edge algorithm for localizing the plasmapause from IMAGE EUV data, paper presented at the Huntsville Modeling Workshop '04, Huntsville, Ala.

Wang, C., T. S. Newman, and D. L. Gallagher (2006), Synthesis of 3D model of a magnetic field-influenced body from a single image, paper presented at Third International Symposium on 3D Data Processing, Visualization and Transmission, IEEE, Chapel Hill, N. C.

Wang, C., T. S. Newman, and D. L. Gallagher (2007), Plasmapause equatorial shape determination via the Minimum L algorithm: Description and evaluation, *J. Geophys. Res.*, *112*, A12201, doi:10.1029/2006JA012202.

Yoshikawa, I., et al. (2008), Telescope of extreme ultraviolet (TEX) onboard SELENE: Science from the Moon, *Earth Planets Space*, *60*(4), 407–416.

B. Chen and F. He, Changchun Institute of Optics, Fine Mechanics and Physics, Chinese Academy of Sciences, 3888 Dongnanhu Rd., Changchun 130033, China.

M.-C. Fok, NASA Goddard Space Flight Center, Code 673, Greenbelt, MD 20771, USA.

X. X. Zhang (corresponding author), National Center for Space Weather, China Meteorological Administration, No. 46 Zhongguancun Nandajie, Haidian District, Beijing 100081, China. (xxzhang@cma.gov.cn)